Title

Quantitative intensity measurement of equal thickness fringes in Si and MgO crystal images with an energy-filtering transmission electron microscope using an imaging plate

Authors

Koji Nishio[1,*]**, Toshiyuki Isshiki**[1] **and Makoto Shiojiri**[1,2]

[1]Department of Electronics and Information Science, Kyoto Institute of Technology,

Matsugasaki, Sakyo-ku, Kyoto 606-8585 and

[2]Department of Anatomy, Kanazawa Medical University,

Uchinada, Ishikawa 920-0293, Japan

[*]To whom correspondence should be addressed. E-mail: knishio@dj.kit.ac.jp

Running title

Quantitative Measurement of Equal Thickness Fringes of Si and MgO

Keywords

electron diffraction intensity, quantitative measurement, energy-filtering TEM,

imaging plate, dynamical diffraction theory, complex potential

Total number of pages

22

Total number of figures

7

Abstract

Quantitative measurement of intensity profiles of equal thickness fringes has been carried out in Si and MgO crystal images with an energy-filtering transmission electron microscope using an imaging plate. The crystals have a 90° wedge-shape with $\{110\}$ surfaces for Si and with $\{100\}$ surfaces for MgO, and are observed under the exact axial incidence of a 200 keV electron beam along the [100] axis for Si and along the $[1\bar{1}0]$ axis for MgO. The intensities are measured in bright field and 022 and 040 dark field images for Si, and in bright field and 111, 002, 220, 113, 222, and 004 dark field images for MgO, with and without an energy slit having ± 5 eV energy width for incident electrons. The intensity profiles obtained from the images are presented as standard experimental data for calculation of electron diffraction intensities. A few simulation programs for high-resolution transmission electron microscopy are checked by comparing the calculated diffraction intensities with the experimental data. The complex potential suitable for matching the data is discussed.

Introduction

High-resolution transmission electron microscopy (HRTEM) has been established as a method to analyze nano-structural materials with atomic scale resolution, supported by the advance of a transmission electron microscope (TEM) and its attachments. In particular, the development of detectors such as an imaging plate [1] and a slow-scan CCD camera [2], which can record an image intensity as digital data with high sensitivity, good linearity and wide dynamic range, has opened up quantitative analysis of HRTEM images and electron diffraction patterns. We have pointed out the possibility of a quantitative HRTEM using some computer experiments in which the images were calculated for InGaAs/InP crystals containing various diffuse interfaces [3] and for InP crystals using various slice thicknesses and crystal potentials [4]. We have also reported

quantitative agreement between the observed and calculated HRTEM images of the [001] InP crystals [5].

The quantitative analysis of experimental data depends entirely on the simulation. Therefore an objective inspection of the simulation program is indispensable for its accuracy. A general simulation program calculates the crystal potential evaluated from atomic scattering factors [6–8], the scattering process in the crystal using a dynamical diffraction theory such as the multi-slice method [9, 10] or the Bethe method [11], and the imaging process by the objective lens on the basis of electron optics, such as the partial coherent imaging theory [12]. These theories contain various approximations and there is a possibility that the programs have bugs or errors. In fact, the results of the calculation of dynamical diffraction intensity by various programs do not always agree with each other [13]. Although mutual comparison of various programs may be effective to find out the bugs, to make the calculated results consistent is not the final aim. The comparison with the reliable experimental data and the subsequent feedback to the theories are still more important.

Equal thickness fringes in a wedge-shaped crystal image are a direct representation of dynamical electron diffraction intensity. Therefore, many investigations were carried out on the basis of the measurement of the equal thickness fringe intensities [14–21], and they have contributed to the improvement of the dynamical electron diffraction theory and the evaluation of the structure factor of the crystals. These experiments were, however, carried out on the two-beam excited Bragg condition, and not on the multi-beam excited zone axis condition which is used in the usual HRTEM work. In a previous paper, we have reported the dynamical diffraction intensity profiles obtained from a GaAs and an InP crystal using a slow-scan CCD camera under the [100] zone axis condition and have compared them with the calculated intensities based on the multi-slice method [22]. The paper has pointed out that the calculated intensities,

which ignored the contribution of inelastically scattered electrons to the equal thickness fringe intensities, agree with the corresponding experimental profiles at thinner region than 20 nm in specimen thickness.

The aim of the present study was to provide reliable and standard experimental data of zero-loss filtered intensity profiles as well as unfiltered ones of equal thickness fringes from a Si crystal as a typical simple substance and a MgO crystal as a typical ionic crystal under the zone axis condition. Kamiya *et al.* [20, 21] indicated that in a small angle region the contribution of inelastically scattered electrons is mainly caused by plasmon excitation rather than phonon excitation. Measurement of zero-loss filtered intensity profiles using an energy-filtering TEM enables us to cut the contribution of inelastically scattered electrons due to plasmon excitation out of the profiles. After comparison between the simulated results using a few programs is presented, a trial is also shown where the simulated results are checked with respect to the obtained experimental data, using various crystal potentials.

Experimental

Si single crystals (diamond-type, $a = 0.54307$ nm) having a 90° wedge-shape were prepared by cleaving a Si (001) wafer along the $\{110\}$ planes and were mounted on a specimen holder for TEM. MgO single crystals (NaCl-type, $a = 0.42112$ nm), having the $\{100\}$ surfaces, were prepared by burning Mg in air and were collected on a carbon-coated grid, with holes, for TEM. The crystal orientations, [100] for Si and $[1\bar{1}0]$ for MgO, were exactly adjusted and confirmed by Kikuchi lines and by symmetry of the intensities of diffraction spots. All images were taken under these axially illuminated conditions at room temperature. The edge of the specimen along the [001] axis has a 90° wedge-shape with the (110) and $(\bar{1}10)$ surfaces for Si and with the (100) and (010) surfaces for MgO in these crystal orientations. Thus, the thickness t can be derived

as a function $t = 2x$ of the distance x from the edge.

The bright field images and the 022 and 040 dark field images for Si, and the bright field images and the 111, 002, 220, 113, 222, and 004 dark field images for MgO were recorded at a direct magnification of more than 200,000 on the imaging plates, whose pixel size is 25 μm. The data can thereby be read out by a spatial resolution of 0.125 nm or less on the specimen. Multi-beam lattice fringes were recorded under the same condition without the objective aperture and were used to calibrate the magnification of the images. The incident beam intensity was measured in a vacuum region out of the crystal for the bright field images, and it was measured after removing the objective aperture for the dark field images. The intensity of the equal thickness fringes was then normalized with respect to the incident beam intensity. Zero-loss filtered images were observed with JEM-2010FEF ($C_s = 1.0$ mm) and JEM-2010EF ($C_s = 3.3$ mm) TEMs equipped with an Ω-type energy filter. The accelerating voltage was 200 kV, and an energy slit was set so as to cut off inelastically scattered electrons with energy loss larger than 5 eV. Unfiltered images were observed with the above microscopes and a JEM-2010 ($C_s = 0.5$ mm) TEM operated at 200 kV.

The multi-slice simulation program to be checked by the experimental data is the one used in our routine HRTEM work [4]. Scattering factors were calculated using the Doyle and Turner expression [7] except for the one for O^{2-}, which was used by Tanji *et al.* [23]. It was confirmed from multi-slice calculation that the image of the flat crystal represents the contrast of the position with corresponding thickness in the image of the wedge-shaped crystal [24]; therefore, the flat crystal model was used for the calculation. Each layer of the multi-slice calculation was normal to the incident direction and contained only the atoms on the same height with respect to the incident electron beam, *i. e.*, $a/4$ for Si and $(a/\sqrt{2})/2$ for MgO were applied to the slice thickness, whose propriety was checked in the previous paper [4]. For reference, calculations

with two packaged programs were also carried out. One of them is MacHREM, which is also based on the multi-slice method originally developed by Ishizuka [12, 25], and the other is the on-line version of EMS [26], which is based on the Bethe method developed by Stadelmann.

Results and discussion

Intensity profiles of equal thickness fringes

Figure 1 shows an example of zero-loss filtered bright field TEM images of a $[1\bar{1}0]$ MgO crystal, recorded on an imaging plate. The areas enclosed by rectangles are sampling areas, where the intensity was averaged over a width of 100 nm along the *c* axis. The width corresponds to 800 pixels on the imaging plate when the observed magnification is 200,000. The averaged intensity of the image was then normalized to the incident beam intensity, which was measured in a vacuum region out of the crystal. Because of quantum noise in each pixel of the image, both the averaged intensity and the incident beam intensity have a standard deviation to the amount of several percents of the intensities. A final intensity profile was obtained by averaging the normalized profiles of several images.

The normalized intensities of the equal thickness fringes of Si, MgO (zero-loss filtered) and MgO (unfiltered) are presented in Tables 1-3 at intervals of 2 nm in thickness, respectively. The corresponding intensity profiles for Si and MgO are shown in Figs. 2 and 3, respectively. Since the magnification of the images was calibrated by the lattice fringes on the multi-beam images, the error in the specimen thickness caused by inaccuracy of the magnification is negligible. The total error in the intensity including the above-mentioned quantum noise is indicated by error bars in Figs. 2 and 3 at intervals of 5 nm in thickness. The profiles of Si (Fig. 2) are influenced by the amorphous surface layer, 1 nm thick, and the profiles of the 222 and 004 dark field images of MgO (Figs. 3f and 3g) are influenced by specimen drift. The former was ignored in this

measurement, although it should be eliminated in an experimental procedure. The latter shows the difficulty in measuring the intensity weaker than 1 % with respect to the incident intensity, even if the intensity was measured using the imaging plate. As the incident beam is limited up to about 10^{-7} A/m^2, to avoid irradiation damage, and the detectability of the imaging plate is 10^{-10} C/m^2, an exposure time to record the intensity up to 1 % of the maximum intensity for such weak images becomes longer than 10 s, which is too long to avoid specimen drift.

Comparing the zero-loss filtered intensity profiles (solid lines in Figs. 2 and 3) with the unfiltered ones (dashed lines), it is obvious that all corresponding profiles have similar figures. The ratio of the zero-loss filtered intensity to the unfiltered intensity tends to decrease with increasing thickness on the whole, although it is not always proportional to the thickness because of multiple scattering in crystal. For example, in the 000 profiles of Si and MgO, the ratio, which is about 90 % at a thickness of 10 nm, approximately decreases to 70 % and 60 % at thicknesses of 50 nm and 90 nm, respectively.

Figure 2 reveals that the incident electrons to the [100] oriented Si crystal are mostly distributed to the $\{022\}$ diffracted waves and the transmitted wave (or the 000 diffracted wave), accompanied by decrease in intensity with increase in thickness due to inelastic scattering. On the other hand, as shown in Figs. 3a-3c, the incident electrons to the $[1\bar{1}0]$ oriented MgO crystal are mostly distributed to the transmitted wave and the $\{111\}$ diffracted waves as well as the $\{002\}$ diffracted waves. The first peak at 23 nm and the fourth peak at 88 nm of the 000 profile shown in Fig. 3a are weak in intensity and it is one of notable characteristics of the intensity profiles of MgO as mentioned in the following section.

Comparison between calculated intensities

Prior to the comparison between the experimental and the calculated intensity, calculations have been carried out with three kinds of simulation programs, *i. e.*, our program (abbreviated as P1) and MacHREM (P2) based on the multi-slice method, and EMS on-line (P3) based on the Bethe method. P1 and P3 use scattering factors evaluated using Doyle and Turner expression [7], while P2 uses scattering factors from international tables [6]. The calculated intensities of the [100] Si and the $[1\bar{1}0]$ MgO, taking no account of temperature effect and inelastic scattering, are indicated in Figs. 4 and 5, respectively. In order to evaluate the correspondence of the calculated intensities, the correlation coefficient $r = \frac{s_{ab}}{s_a \cdot s_b}$ between profiles a and b was calculated, where s_a and s_b are standard deviations of the two profiles a and b, respectively, and s_{ab} is covariance between them. The intensity profiles for the Si are consistent with each other as shown in Figs. 4a-4c, and high correlation coefficients of $r = 0.996 \sim 0.999$ were obtained between these intensity profiles. For the MgO shown in Figs. 5a-5g, there is a small discrepancy between the profiles and the correlation coefficient decreased to $0.980 \sim 0.993$.

Results calculated by P1 using other scattering factors [8] were slightly different from the results shown in Figs. 4 and 5. It was also confirmed by the calculations with P1 and P3 that inadequate parameters such as insufficient number of excited waves and large slice thickness give different results. Therefore, all the calculations mentioned above were carried out under the same conditions as good as possible within the limit of the programs. The small difference, which appears between P1 and P2 might be caused by using different scattering factors. The difference between P1 (P2) and P3 seems to be caused by the difference in algorithm between the multi-slice method and Bethe method, which is not clear at the present. The discrepancy is, however, insignificant on the comparison with the experimental results.

Comparison between experimental and calculated intensity

The positions of the peaks in the calculated profiles shown in Figs. 4a-4c slightly disagree with those in the experimental profiles of Si shown in Fig. 2. The position difference ranges between -2 nm and 4 nm. The intensities of the calculated profiles also disagree with those of the zero-loss filtered experimental profiles, because temperature effect and inelastic scattering of electrons are neglected in these calculations for the profiles. The inelastic scattering decreases the total intensity of elastically scattered electrons [27] and also contributes to the image formation as well as the background [28]. The former effect is unavoidable and essential on the electron scattering in crystal, while the latter effect can be almost removed using the energy filter as shown in Figs. 2 and 3. To take account of the inelastic scattering in crystal, a phenomenological calculation, where the inelastic scattering is treated as an absorption effect, was carried out with our multi-slice program P1 by utilizing complex potential [29]. For simplification, the constant ratio of imaginary part of the complex potential, V_{im}, to real part, V_{re}, varying from 0 % to 10 % at intervals of 1 %, was used for a calculation similar to that used by Hashimoto *et al.* [27]. As shown in Fig. 4d, the diffraction intensity is decreasing with increasing ratio, $\frac{V_{im}}{V_{re}}$. In addition, temperature factor, B, was also varied from 0 nm^2 to 1×10^{-2} nm^2 at intervals of 5×10^{-4} nm^2 for each $\frac{V_{im}}{V_{re}}$. There are no appreciable changes in the positions of the peaks for all B, while the intensity increases for the 000 profile and it decreases for the 022 and the 040 profiles with increasing B. The best correspondence was obtained at $\frac{V_{im}}{V_{re}} = 4$ % and $B = 4.5 \times 10^{-3}$ nm^2 with the correlation coefficient r above 0.95, as shown in Fig. 6. It is confirmed by this calculation that $B = 4.5 \times 10^{-3}$ nm^2, which is the value of the temperature factor appearing in international tables [30], is the most probable value. The reciprocal of mean absorption coefficient estimated from this calculation is 71 nm. Since the positions of the peaks in the calculated profiles in Fig. 6 change scarcely with varying ratio $\frac{V_{im}}{V_{re}}$ as shown in

Fig. 4d, the discrepancy of the positions of the peak between the experimental and the calculated profiles still remains ranging between -2 nm and 4 nm. In this calculation, all of the inelastically scattered electrons are assumed to be cut off by the energy slit and the objective aperture. Some of phonon scattered electrons, however, pass through them and contribute to the image formation. In addition, the ratio of V_{im} to V_{re} depends on the scattering angle [31], although the constant ratio obtained from this calculation seems reasonable comparing with theoretical values by Radi [32]. It is preferable for more accurate simulation to include such effects as the contribution of the inelastically scattered, survived electrons to the image formation and the dependence of the ratio of V_{im} to V_{re} on the scattering angle.

On the other hand, there are some differences in shape as well as in intensity between the zero-loss filtered experimental profiles of MgO in Fig. 3 and the calculated profiles in Fig. 5a-5g. For instance, the first peak at 23 nm is weaker than the second one at 45 nm in Fig. 3a, while the strongest peak is the third one and the first one is strong and comparable with the second one in Fig. 5a. The difference in the 111 profiles is also remarkable; the second peak at 43 nm is weaker than the first one at 22 nm in Fig. 3b, while the second one is strong and comparable with the first one in Fig. 5b. The discrepancy remains although the same phenomenological calculations as that for Si have been carried out. Crystal potential used in these calculations was derived from the scattering factors for neutral atoms [7]. Then, similar calculations were performed using the crystal potentials derived from the scattering factors for Mg^{2+} [7] and O^{2-} [23]. Significant changes appear in the 000 and 111 profiles. This reflects the fact that the scattering factors for ions are different from those for neutral atoms in the region of small scattering angle. The heights of the peaks in the 000 profile calculated using the ion scattering factors approach those in the experimental profile in Fig. 3a, as seen in Fig. 5h. For the 111 profile, however, the positions of some peaks are shifted, and consequently, the correlation

coefficient to the experimental profile is worse than that for the profile calculated with neutral atoms. That is, the correlation coefficient of the 000 profile increases from 0.95 to 0.97, but that of the 111 profile decreases from 0.92 to 0.78.

It has been reported that $Mg^{2+}O^{2-}$ is better than $Mg^{0}O^{0}$ for calculating the crystal potential of MgO in comparison between the calculated and measured structure factors [33], and the recent molecular orbital calculation suggests that net charge of Mg and O in MgO crystal is 1.83 rather than 2 [34]. In order to take the effect into account, the calculation was carried out with trial crystal potentials, $V_{mix}(= (1-x)V_{neu} + xV_{ion})$, which were derived from a mixture of the scattering factors for neutral atoms, V_{neu}, and those for ions, V_{ion}. The mixing rate of the scattering factors for ions, x, was varied from 0 % to 100 % at intervals of 5 %, and the ratio of V_{im} to V_{re} was also varied from 0 % to 10 % at intervals of 1 % for each mixed potential. Both the temperature factors, B, for Mg and O were assumed to be equal and fixed to 0 nm^2 or 3.0×10^{-3} nm^2 [35]. The best correlation coefficients between the experimental and calculated profiles were obtained at $B = 3.0 \times 10^{-3}$ nm^2, $x = 75$ % and $\frac{V_{im}}{V_{re}} = 4$ %. The corresponding calculated profiles with the zero-loss filtered experimental profiles are shown in Fig. 7. Although a high correlation coefficient of $r = 0.997$ is obtained for the 000 profile, it seems that the discrepancy between the experimental and calculated profiles for the 111 ($r = 0.892$) and 002 profiles ($r = 0.863$) is serious. In case of MgO, the position of the peaks as well as the intensity was influenced by the temperature factor. The position of the peaks of the 002 profile agreed with the experimental one at $B = 0$ nm^2 rather than $B = 3.0 \times 10^{-3}$ nm^2. The highest correlation coefficient for the 111 profile was obtained at $x = 65$ % and $\frac{V_{im}}{V_{re}} = 3$ %. These results may suggest that different temperature factors for individual elements, taking account of anisotropic thermal vibration, should be taken in the calculation; in addition to the other effects such as the contribution of the inelastically scattered electrons and the dependence of the ratio

of V_{im} to V_{re} on the scattering angle, which were pointed out in the case of Si.

Conclusion

Bright field and dark field TEM images of both 90° wedge-shaped Si and MgO crystals were recorded on imaging plates under the zone-axis incidence condition. Intensity profiles obtained from zero-loss filtered and unfiltered equal thickness fringes are presented for the 000, 022, and 040 reflections of [100] Si and for the 000, 111, 002, 220, 113, 222, and 004 reflections of $[1\bar{1}0]$ MgO. Contribution of inelastically scattered electrons except for phonon excitation to the images is shown by comparing between zero-loss filtered and unfiltered intensity profiles.

It has been revealed that the results, which were calculated with a few simulation programs written in the based on the multi-slice method or the Bethe method, are almost coincident with each other. Then, comparison between the experimental profiles and the calculated profiles was carried out. In the calculations for Si taking no account of inelastic scattering, the position of peaks almost agrees with the experimental one but the intensity of them disagrees. The agreement improves to 0.95 in correlation coefficient by introducing a complex potential of $(1+0.04i)V_{re}$ and a temperature factor of $B = 4.5 \times 10^{-3}$ nm^2 in the calculation. For MgO crystal, the calculation assuming neutral atoms could not account for the experimental result, giving a poor agreement in the position as well as the intensity of peaks. The agreement improved when the calculation was performed using the complex potential, taking account of a mixture of the both scattering factors for neutral atoms and ions.

Acknowledgements

The authors wish to express their sincere thanks to Drs. Eiji Okunishi, Tetsuo Oikawa and Masahiro Kawasaki, JEOL Ltd., for their careful experiments with the energy-filtering TEMs.

Special thanks are extended to Dr. Kazuo Ishizuka for his thoughtful suggestions especially for an importance of thermal vibration and to Dr. Kyozaburo Kambe for critical reading of the manuscript. The authors appreciate that Prof. Pierre A. Stadelmann, EPFL, has opened his EMS software package to the public on the internet and that Mr. Susumu Enomoto, ENOMOTO A&V Co., Ltd., the distributor of MacHREM, has lent us the programs for this research.

Appendix

It has been revealed that better correlation coefficients were obtained at $x = 100$ % (and $\frac{V_{im}}{V_{re}} = 4$ %) when another expression of structure factor for Mg^{2+} and O^{2-} ions [36] were applied to the calculation. It seems that the expression reflects well the structure factor for Mg^{2+} and O^{2-} ions in MgO crystal.

References

1 Mori N, Oikawa T, Harada Y, and Miyahara J (1990) Development of the imaging plate for the transmission electron microscope and its characteristics. *J. Electron Microsc.* **39**: 433–436.

2 Mooney P E, Fan G Y, Meyer C E, Truong K V, Bui D B, and Krivanek O L (1990) Slow-scan CCD camera for transmission electron microscopy. In: *Proceedings of the XIIth International Congress for Electron Microscopy*, eds. L D Peachey and D B Williams, volume 1, pp. 164–165 (San Francisco Press, San Francisco).

3 Shiojiri M, Isshiki T, Nishio K, Tsujikura M, Saijo H, Takahashi Y, Ohtsuka N, and Yabuuchi Y (1992) Quantitative structure images of interfaces in InGaAs/InP multilayer heterostructures. *J. Electron Microsc.* **41**: 438–444.

4 Nishio K, Isshiki T, Saijo H, and Shiojiri M (1994) Multi-slice calculation for InP crystals using different slices. *Ultramicroscopy* **54**: 301–309.

5 Oikawa T, Kawasaki M, Kondo Y, Yabuuchi Y, Takahashi Y, Isshiki T, and Shiojiri M (1993) Quantitative analysis of high resolution images of InGaAs/InP multilayer heterostructure. In: *Abstracts of 49th Annual Meeting of Japanese Society of Electron Microscopy: J. Electron Microsc.* **42**, p. 254.

6 Ibers J A and Hamilton W C, eds. (1974) *International tables for X-ray crystallography*, volume IV. Revised and supplementary tables to volumes II and III (Kynoch Press, Birmingham, England).

7 Doyle P A and Turner P S (1968) Relativistic Hartree-Fock X-ray and electron scattering factors. *Acta Cryst.* **A 24**: 390–397.

8 Weickenmeier A and Kohl H (1991) Computation of absorptive form factors for high-energy electron diffraction. *Acta Cryst.* **A47**: 590–597.

9 Cowley J M and Moodie A F (1957) The scattering of electrons by atoms and crystals I. A new theoretical approach. *Acta Cryst.* **10**: 609–619.

10 Goodman P and Moodie A F (1974) Numerical evaluation of N-beam wave functions in electron scattering by the multi-slice method. *Acta Cryst.* **A30**: 280–290.

11 Bethe H (1928) Theorie der beugung von elektronen an kristallen. *Ann. d. Phys.* **87**: 55–129.

12 Ishizuka K (1980) Contrast transfer of crystal images in TEM. *Ultramicroscopy* **5**: 55–65.

13 Ishizuka K, Endoh H, Kuwano N, Shindo D, Tanaka N, and Horiuchi S (1994) Standardization of the computer simulation of high-resolution transmission electron microscope image,

I. Calculation of diffraction amplitudes by the multi-slice method. *Electron Microscopy (Japanese)* **29**: 141–143.

14 Kohra K and Watanabe H (1961) Measurement of anomalous absorption coefficients of electrons for MgO crystals. *J. Phys. Soc. Jpn* **16**: 580–581.

15 Watanabe H, Fukuhara A, and Kohra K (1962) Measurement of mean and anomalous absorption coefficients of electrons in MgO crystals by the use of electron micrographic images. *J. Phys. Soc. Jpn* **17**: Suppl. B–II, 195–199.

16 Kamiya Y (1963) Effect of inelastic scattering on mean and anomalous absorption coefficients of electrons in magnesium oxide crystals studied by electron microscope. *Jpn J. Appl. Phys.* **2**: 386–393.

17 Hashimoto H (1964) Energy dependence of extinction distance and transmissive power for electron waves in crystals. *J. Appl. Phys.* **35**: 277–290.

18 Uyeda R and Nonoyama M (1965) Electron microscope study on the extinction and absorption of 100 kV electrons in magnesium oxide single crystals. *Jpn J. Appl. Phys.* **4**: 498–512.

19 Ichimiya A (1969) Mean and anomalous absorption coefficients of electrons for magnesium oxide single crystal. *Jpn J. Appl. Phys.* **8**: 518–529.

20 Kamiya Y and Goto T (1980) Extinction contour in electron microscopic images of crystals. *J. Phys. Soc. Jpn* **49**: 1475–1479.

21 Kamiya Y, Nakai Y, and Masuda E (1981) Absorption coefficients of electrons in crystals. *Acta Cryst.* **A37**: 485–488.

22 Nishio K, Kakibayashi H, Isshiki T, Saijo H, and Shiojiri M (1994) Intensity measurement of equal-thickness fringes in TEM images of wedge-shaped GaAs and InP crystals by a slow-scan CCD camera. *J. Electron Microsc.* **43**: 198–202.

23 Tanji T, Masaoka H, and Ito J (1989) Simulation of high resolution electron microscope images of a wedge-shaped crystal, MgO. *J. Electon Microsc.* **38**: 409–414.

24 Yabuuchi Y, Takahashi Y, Ohtsuka N, Isshiki T, Tsujikura M, Saijo H, and Shiojiri M (1991) High-resolution transmission electron microscopy observations of InGaAs/InP multilayer heterostructures. *Phys. Stat. Sol. (a)* **127**: 385–396.

25 Ishizuka K and Uyeda N (1977) A new theoretical and practical approach to the multislice method. *Acta Cryst.* **A33**: 740–749.

26 Stadelmann P A (1987) EMS - a software package for electron diffraction analysis and HREM image simulation in materials science. *Ultramicroscopy* **21**: 131–146.

27 Hashimoto H, Howie A, and Whelan M J (1962) Anomalous electron absorption effects in metal foils: theory and comparison with experiment. *Proc. Royal Soc.* **A269**: 80–103.

28 Kamiya Y and Uyeda R (1961) Effect of incoherent waves on the electron microscopic images of crystals. *J. Phys. Soc. Jpn* **16**: 1361–1366.

29 Yoshioka H (1957) Effect of inelastic waves on electron diffraction. *J. Phys. Soc. Jpn* **12**: 618–628.

30 Macgillavry C H and Rieck G D, eds. (1968) *International tables for X-ray crystallography*, volume III. Physical and chemical tables (Kynoch Press, Birmingham, England).

31 Humphreys C J and Hirsch P B (1968) Absorption parameters in electron diffraction theory. *Phil. Mag.* **18**: 115–122.

32 Radi G (1970) Complex lattice potentials in electron diffraction calculated for a number of crystals. *Acta Cryst.* **A26**: 41–56.

33 Fukamachi T and Hosoya S (1971) Electron state of an O^{-2} atom in MgO. *J. Phys. Soc. Jpn* **31**: 980–989.

34 Xu Y N and Ching W Y (1991) Self-consistent band structures, charge distributions, and optical-absorption spectra in MgO, α-Al_2O_3, and $MgAl_2O_4$. *Phys. Rev. B* **43**: 4461–4472.

35 Goodman P (1971) The influence of temperature on the MgO zone-axis pattern. *Acta Cryst.* **A27**: 140–147.

36 Peng L M (1998) Electron scattering factors of ions and their parameterization. *Acta Cryst.* **A54**: 481–485.

Figure captions

Fig. 1 A zero-loss filtered bright field TEM image of $[1\bar{1}0]$ MgO crystal having a 90° wedge shape, recorded on an imaging plate. The intensity in the areas enclosed by rectangles was averaged over along the *c* axis.

Fig. 2 Dependence of diffraction intensity on crystal thickness for $[100]$ Si crystal axially illuminated by a 200 keV electron beam. The intensity is normalized with respect to the incident beam intensity. (a-c) Intensity profiles of bright field, 022 dark field and 040 dark field with (solid line) and without (dashed) an energy slit of ± 5 eV in width, respectively.

Fig. 3 Dependence of diffraction intensity on crystal thickness, for $[1\bar{1}0]$ MgO crystal axially illuminated by a 200 keV electron beam. The intensity is normalized with respect to the incident beam intensity. (a-g) Intensity profiles of bright field, and 111, 002, 220, 113, 222, and 004 dark fields with (solid line) and without (dashed) an energy slit of ± 5 eV in width, respectively.

Fig. 4 (a-c) Diffraction intensities for 000, 022, and 040 of Si, calculated with programs P1 (solid line) and P2 (dashed) based on the multi-slice method and program P3 (dotted) based on the Bethe method, respectively. (d) Dependence of diffraction intensity on the ratio of V_{im} to V_{re}. Diffraction intensities for 000 of Si calculated with P1, for the ratio, V_{im}/V_{re}, varying from 0 % to 5 % at intervals of 1 %, are indicated.

Fig. 5 (a-g) Diffraction intensities for 000, 111, 002, 220, 113, 222, and 004 of MgO, calculated with programs P1 (solid line), P2 (dashed) and P3 (dotted), respectively.
(h) Diffraction intensities for 000 of MgO calculated with P1, using scattering factors for neutral atoms and ions.

Fig. 6 (a) Dependence of the correlation coefficient between the experimental and calculated intensity profiles for Si, on the ratio of V_{im} to V_{re}. (b-d) Experimental intensity profiles (solid line) shown in Fig. 2 and calculated intensity profiles (dashed), for 000, 022, and 040 of Si, respectively, at $V_{im}/V_{re} = 4$ % and $B = 4.5 \times 10^{-3}$ nm^2. The correlation coefficients between the profiles, r, are indicated.

Fig. 7 (a-g) Experimental intensity profiles (solid line) shown in Fig. 3 and calculated intensity profiles (dashed) best matching with the experimental ones (see text), for 000, 111, 002, 220, 113, 222, and 004 of MgO, respectively. The correlation coefficients, r, are also indicated.

Table 1 Normalized intensity of equal thickness fringes in both zero-loss filtered images and unfiltered images of Si, for the bright field of 000 and the dark fields of 022 and 040.

Crystal thickness	Normalized intensity					
	Zero-loss filtered			Unfiltered		
t [nm]	000	022	040	000	022	040
0	9.21E-01	1.50E-03	6.21E-04	9.64E-01	3.22E-03	9.32E-04
2	8.90E-01	4.46E-03	1.35E-03	9.37E-01	7.96E-03	1.88E-03
4	8.25E-01	1.39E-02	4.11E-03	8.78E-01	1.94E-02	4.99E-03
6	7.30E-01	2.79E-02	7.57E-03	7.89E-01	3.61E-02	8.69E-03
8	6.19E-01	4.50E-02	9.73E-03	6.77E-01	5.57E-02	1.11E-02
10	5.08E-01	6.21E-02	9.50E-03	5.65E-01	7.54E-02	1.10E-02
12	4.12E-01	7.68E-02	8.43E-03	4.68E-01	9.11E-02	1.04E-02
14	3.40E-01	8.46E-02	7.99E-03	3.97E-01	1.01E-01	1.04E-02
16	2.99E-01	8.45E-02	8.60E-03	3.59E-01	9.96E-02	1.14E-02
18	2.93E-01	7.58E-02	1.00E-02	3.58E-01	9.03E-02	1.28E-02
20	3.18E-01	6.25E-02	1.11E-02	3.93E-01	7.52E-02	1.36E-02
22	3.70E-01	4.76E-02	1.05E-02	4.58E-01	5.89E-02	1.28E-02
24	4.34E-01	3.29E-02	8.06E-03	5.36E-01	4.23E-02	1.01E-02
26	4.99E-01	2.00E-02	4.79E-03	6.15E-01	2.81E-02	6.80E-03
28	5.50E-01	1.12E-02	2.69E-03	6.79E-01	1.81E-02	4.61E-03
30	5.78E-01	6.63E-03	2.15E-03	7.17E-01	1.32E-02	4.01E-03
32	5.76E-01	7.28E-03	2.72E-03	7.21E-01	1.46E-02	4.53E-03
34	5.49E-01	1.34E-02	3.58E-03	6.94E-01	2.23E-02	5.51E-03
36	5.02E-01	2.35E-02	4.09E-03	6.41E-01	3.46E-02	6.20E-03
38	4.39E-01	3.56E-02	4.36E-03	5.69E-01	4.97E-02	6.75E-03
40	3.69E-01	4.71E-02	5.24E-03	4.90E-01	6.39E-02	7.93E-03
42	3.03E-01	5.52E-02	7.03E-03	4.12E-01	7.46E-02	9.97E-03
44	2.47E-01	5.86E-02	9.37E-03	3.47E-01	7.96E-02	1.23E-02
46	2.08E-01	5.77E-02	1.10E-02	3.02E-01	7.96E-02	1.43E-02
48	1.94E-01	5.30E-02	1.11E-02	2.87E-01	7.45E-02	1.54E-02
50	2.00E-01	4.57E-02	9.91E-03	2.99E-01	6.67E-02	1.45E-02
52	2.27E-01	3.71E-02	7.62E-03	3.35E-01	5.64E-02	1.24E-02
54	2.65E-01	2.74E-02	5.15E-03	3.86E-01	4.46E-02	9.78E-03
56	3.06E-01	1.83E-02	3.62E-03	4.44E-01	3.33E-02	7.86E-03
58	3.45E-01	1.13E-02	3.19E-03	4.97E-01	2.42E-02	6.91E-03
60	3.70E-01	7.32E-03	3.13E-03	5.36E-01	1.92E-02	6.43E-03
62	3.81E-01	7.26E-03	2.97E-03	5.57E-01	1.88E-02	6.06E-03
64	3.76E-01	1.03E-02	2.70E-03	5.55E-01	2.27E-02	5.72E-03
66	3.54E-01	1.52E-02	2.65E-03	5.31E-01	2.93E-02	5.75E-03
68	3.18E-01	2.07E-02	3.45E-03	4.87E-01	3.68E-02	6.77E-03
70	2.75E-01	2.58E-02	5.15E-03	4.31E-01	4.39E-02	8.74E-03
72	2.28E-01	2.97E-02	6.80E-03	3.68E-01	4.97E-02	1.10E-02
74	1.86E-01	3.21E-02	7.76E-03	3.12E-01	5.40E-02	1.26E-02
76	1.53E-01	3.34E-02	7.67E-03	2.67E-01	5.65E-02	1.29E-02
78	1.34E-01	3.30E-02	6.69E-03	2.41E-01	5.68E-02	1.22E-02
80	1.30E-01	3.05E-02	5.41E-03	2.36E-01	5.39E-02	1.10E-02
82	1.40E-01	2.59E-02	4.57E-03	2.49E-01	4.81E-02	1.00E-02
84	1.61E-01	2.02E-02	4.35E-03	2.80E-01	4.07E-02	9.51E-03
86	1.87E-01	1.46E-02	4.39E-03	3.19E-01	3.29E-02	9.19E-03
88	2.14E-01	9.81E-03	4.10E-03	3.62E-01	2.63E-02	8.75E-03
90	2.38E-01	6.75E-03	3.38E-03	4.00E-01	2.19E-02	8.06E-03
92	2.52E-01	5.44E-03	2.70E-03	4.28E-01	1.97E-02	7.33E-03
94	2.56E-01	5.70E-03	2.45E-03	4.39E-01	1.97E-02	6.93E-03
96	2.48E-01	7.22E-03	2.92E-03	4.30E-01	2.17E-02	7.23E-03
98	2.29E-01	9.69E-03	3.82E-03	4.06E-01	2.52E-02	8.23E-03
100	2.01E-01	1.30E-02	4.66E-03	3.66E-01	3.00E-02	9.33E-03

Table 2 Normalized intensity of equal thickness fringes in zero-loss filtered images of MgO, for the bright field of 000 and the dark fields of 111, 002, 220, 113, 222, and 004.

Crystal thickness	Normalized intensity						
	Zero-loss filtered						
t [nm]	000	111	002	220	113	222	004
0	9.86E-01	5.34E-04	2.42E-03	8.81E-04	3.89E-04	3.22E-04	8.54E-04
2	9.01E-01	1.42E-03	1.01E-02	5.49E-03	8.22E-04	1.80E-03	2.60E-03
4	7.76E-01	3.34E-03	2.80E-02	1.50E-02	1.52E-03	6.09E-03	3.52E-03
6	6.04E-01	7.07E-03	6.14E-02	2.59E-02	2.40E-03	7.88E-03	3.34E-03
8	4.12E-01	1.31E-02	1.05E-01	3.09E-02	3.19E-03	6.09E-03	3.43E-03
10	2.58E-01	2.29E-02	1.51E-01	2.78E-02	3.47E-03	4.13E-03	5.16E-03
12	1.37E-01	3.71E-02	1.82E-01	1.89E-02	3.32E-03	5.52E-03	6.41E-03
14	7.46E-02	5.23E-02	1.88E-01	1.00E-02	3.38E-03	8.69E-03	5.43E-03
16	6.70E-02	6.94E-02	1.63E-01	7.32E-03	4.09E-03	8.35E-03	4.02E-03
18	9.17E-02	8.12E-02	1.24E-01	1.02E-02	5.14E-03	5.78E-03	3.42E-03
20	1.26E-01	8.94E-02	8.41E-02	1.22E-02	5.94E-03	3.73E-03	2.94E-03
22	1.46E-01	9.27E-02	5.70E-02	1.07E-02	5.86E-03	3.02E-03	2.24E-03
24	1.46E-01	9.00E-02	4.93E-02	7.11E-03	5.09E-03	2.24E-03	1.88E-03
26	1.28E-01	8.22E-02	5.67E-02	5.18E-03	5.06E-03	2.31E-03	1.89E-03
28	9.95E-02	6.89E-02	7.26E-02	6.41E-03	5.88E-03	3.52E-03	1.91E-03
30	7.32E-02	5.52E-02	8.78E-02	9.74E-03	6.88E-03	3.93E-03	2.04E-03
32	6.04E-02	4.24E-02	9.51E-02	1.30E-02	7.09E-03	2.38E-03	2.42E-03
34	6.92E-02	3.42E-02	9.15E-02	1.43E-02	6.57E-03	1.51E-03	2.81E-03
36	1.01E-01	3.29E-02	7.65E-02	1.27E-02	5.77E-03	3.20E-03	2.73E-03
38	1.51E-01	3.76E-02	5.41E-02	8.41E-03	5.22E-03	5.36E-03	2.32E-03
40	2.04E-01	4.36E-02	3.55E-02	4.66E-03	4.62E-03	4.53E-03	1.80E-03
42	2.47E-01	4.89E-02	3.15E-02	3.87E-03	3.89E-03	2.39E-03	1.43E-03
44	2.69E-01	4.94E-02	4.52E-02	5.82E-03	3.15E-03	1.81E-03	1.47E-03
46	2.65E-01	4.54E-02	6.92E-02	7.54E-03	2.61E-03	1.95E-03	1.82E-03
48	2.38E-01	3.74E-02	9.55E-02	6.94E-03	2.27E-03	2.05E-03	2.16E-03
50	1.97E-01	2.90E-02	1.15E-01	5.05E-03	1.95E-03	3.44E-03	2.66E-03
52	1.50E-01	2.12E-02	1.19E-01	4.41E-03	1.70E-03	5.59E-03	3.63E-03
54	1.06E-01	1.54E-02	1.11E-01	7.34E-03	1.52E-03	5.95E-03	4.56E-03
56	7.89E-02	1.23E-02	9.23E-02	1.20E-02	1.45E-03	3.89E-03	4.42E-03
58	7.13E-02	1.15E-02	7.08E-02	1.59E-02	1.42E-03	2.99E-03	3.55E-03
60	8.47E-02	1.18E-02	4.85E-02	1.62E-02	1.41E-03	4.81E-03	2.95E-03
62	1.15E-01	1.18E-02	3.05E-02	1.35E-02	1.48E-03	7.09E-03	2.87E-03
64	1.53E-01	1.06E-02	1.97E-02	8.94E-03	1.62E-03	5.75E-03	2.58E-03
66	1.87E-01	8.02E-03	1.77E-02	5.55E-03	1.74E-03	3.09E-03	2.10E-03
68	2.07E-01	5.01E-03	2.31E-02	4.39E-03	1.81E-03	1.89E-03	1.77E-03
70	2.08E-01	3.59E-03	3.29E-02	5.43E-03	1.98E-03	2.15E-03	1.64E-03
72	1.91E-01	5.10E-03	3.97E-02	7.07E-03	2.51E-03	2.17E-03	1.56E-03
74	1.61E-01	1.03E-02	4.24E-02	7.74E-03	3.28E-03	1.82E-03	1.67E-03
76	1.26E-01	1.87E-02	4.13E-02	6.87E-03	3.84E-03	2.11E-03	2.12E-03
78	9.33E-02	2.85E-02	3.73E-02	5.05E-03	3.84E-03	2.85E-03	2.44E-03
80	6.91E-02	3.87E-02	3.24E-02	3.82E-03	3.41E-03	3.00E-03	2.29E-03
82	5.51E-02	4.61E-02	2.84E-02	4.24E-03	3.07E-03	2.40E-03	1.86E-03
84	5.02E-02	4.99E-02	2.70E-02	5.48E-03	3.10E-03	2.08E-03	1.56E-03
86	5.10E-02	5.03E-02	2.84E-02	6.22E-03	3.44E-03	2.22E-03	1.47E-03
88	5.26E-02	4.64E-02	3.30E-02	5.82E-03	3.63E-03	2.54E-03	1.59E-03
90	5.24E-02	3.87E-02	3.91E-02	4.92E-03	3.23E-03	2.84E-03	1.80E-03
92	4.85E-02	2.98E-02	4.40E-02	4.57E-03	2.50E-03	3.24E-03	1.92E-03
94	4.22E-02	2.08E-02	4.61E-02	5.16E-03	1.99E-03	3.41E-03	1.95E-03
96	3.65E-02	1.33E-02	4.43E-02	6.01E-03	1.95E-03	2.88E-03	2.01E-03
98	3.38E-02	8.33E-03	3.82E-02	6.66E-03	2.22E-03	1.99E-03	2.06E-03
100	3.72E-02	5.68E-03	2.88E-02	6.45E-03	2.30E-03	1.83E-03	1.99E-03

Table 3 Normalized intensity of equal thickness fringes in unfiltered images of MgO, for the bright field of 000 and the dark fields of 111, 002, 220, 113, 222, and 004.

Crystal thickness	Normalized intensity						
	Unfiltered						
t [nm]	000	111	002	220	113	222	004
0	9.87E-01	2.14E-03	1.12E-03	1.65E-03	1.00E-03	9.33E-04	9.96E-04
2	9.16E-01	3.60E-03	1.04E-02	6.31E-03	1.68E-03	2.92E-03	3.74E-03
4	8.00E-01	6.41E-03	3.30E-02	1.66E-02	2.68E-03	7.08E-03	5.27E-03
6	6.36E-01	1.15E-02	7.58E-02	2.79E-02	3.94E-03	8.64E-03	5.01E-03
8	4.48E-01	1.99E-02	1.34E-01	3.41E-02	5.02E-03	6.66E-03	4.87E-03
10	2.86E-01	3.32E-02	1.91E-01	3.09E-02	5.51E-03	5.24E-03	7.58E-03
12	1.56E-01	5.20E-02	2.32E-01	2.20E-02	5.47E-03	6.78E-03	9.96E-03
14	8.27E-02	7.27E-02	2.33E-01	1.30E-02	5.62E-03	9.72E-03	9.02E-03
16	7.19E-02	9.51E-02	2.01E-01	9.82E-03	6.67E-03	8.98E-03	6.80E-03
18	9.73E-02	1.11E-01	1.50E-01	1.32E-02	8.39E-03	6.47E-03	5.85E-03
20	1.35E-01	1.22E-01	9.99E-02	1.50E-02	9.71E-03	4.65E-03	5.13E-03
22	1.57E-01	1.26E-01	7.18E-02	1.32E-02	9.58E-03	4.02E-03	4.14E-03
24	1.58E-01	1.22E-01	6.87E-02	9.56E-03	8.88E-03	3.48E-03	3.70E-03
26	1.40E-01	1.11E-01	8.36E-02	7.77E-03	8.86E-03	3.73E-03	3.91E-03
28	1.12E-01	9.47E-02	1.09E-01	9.33E-03	9.80E-03	5.06E-03	4.11E-03
30	8.50E-02	7.79E-02	1.32E-01	1.30E-02	1.10E-02	5.44E-03	4.25E-03
32	7.21E-02	6.32E-02	1.39E-01	1.66E-02	1.16E-02	4.00E-03	5.12E-03
34	8.20E-02	5.45E-02	1.35E-01	1.80E-02	1.11E-02	3.36E-03	6.24E-03
36	1.18E-01	5.42E-02	1.11E-01	1.63E-02	1.01E-02	5.20E-03	6.32E-03
38	1.78E-01	6.11E-02	7.95E-02	1.20E-02	9.48E-03	7.28E-03	5.39E-03
40	2.47E-01	7.01E-02	5.54E-02	8.63E-03	8.78E-03	6.29E-03	4.32E-03
42	3.11E-01	7.68E-02	5.37E-02	8.46E-03	7.78E-03	4.37E-03	3.67E-03
44	3.49E-01	7.73E-02	7.68E-02	1.09E-02	6.73E-03	4.07E-03	3.81E-03
46	3.56E-01	7.11E-02	1.16E-01	1.26E-02	5.98E-03	4.40E-03	4.45E-03
48	3.30E-01	6.04E-02	1.58E-01	1.20E-02	5.59E-03	4.62E-03	5.36E-03
50	2.77E-01	4.84E-02	1.91E-01	1.01E-02	5.24E-03	5.75E-03	6.59E-03
52	2.14E-01	3.80E-02	2.05E-01	9.90E-03	4.97E-03	7.83E-03	8.70E-03
54	1.51E-01	3.03E-02	1.96E-01	1.33E-02	4.81E-03	8.42E-03	1.07E-02
56	1.09E-01	2.61E-02	1.70E-01	1.80E-02	4.75E-03	6.67E-03	1.06E-02
58	9.30E-02	2.48E-02	1.29E-01	2.16E-02	4.74E-03	5.99E-03	9.00E-03
60	1.07E-01	2.46E-02	8.77E-02	2.22E-02	4.76E-03	7.66E-03	7.97E-03
62	1.47E-01	2.43E-02	5.66E-02	1.96E-02	4.87E-03	9.92E-03	8.09E-03
64	2.01E-01	2.28E-02	4.14E-02	1.53E-02	5.16E-03	8.61E-03	7.62E-03
66	2.51E-01	2.04E-02	4.17E-02	1.24E-02	5.57E-03	6.13E-03	6.43E-03
68	2.82E-01	1.83E-02	5.36E-02	1.18E-02	6.04E-03	5.01E-03	5.57E-03
70	2.88E-01	1.91E-02	6.87E-02	1.30E-02	6.53E-03	5.27E-03	5.37E-03
72	2.69E-01	2.46E-02	8.14E-02	1.45E-02	7.33E-03	5.33E-03	5.25E-03
74	2.30E-01	3.51E-02	8.73E-02	1.47E-02	8.40E-03	4.96E-03	5.24E-03
76	1.85E-01	4.93E-02	8.52E-02	1.34E-02	9.52E-03	5.10E-03	5.96E-03
78	1.43E-01	6.45E-02	7.74E-02	1.17E-02	1.01E-02	5.81E-03	6.95E-03
80	1.10E-01	7.83E-02	6.84E-02	1.07E-02	9.97E-03	6.07E-03	6.91E-03
82	9.13E-02	8.76E-02	6.00E-02	1.11E-02	9.63E-03	5.74E-03	6.00E-03
84	8.42E-02	9.10E-02	5.64E-02	1.23E-02	9.48E-03	5.50E-03	5.41E-03
86	8.45E-02	8.89E-02	5.89E-02	1.30E-02	9.61E-03	5.67E-03	5.45E-03
88	8.73E-02	8.21E-02	6.50E-02	1.28E-02	9.72E-03	5.92E-03	5.81E-03
90	8.79E-02	7.15E-02	7.34E-02	1.21E-02	9.28E-03	6.25E-03	6.24E-03
92	8.39E-02	5.98E-02	8.18E-02	1.18E-02	8.40E-03	6.66E-03	6.61E-03
94	7.59E-02	4.83E-02	8.84E-02	1.24E-02	7.66E-03	6.92E-03	6.60E-03
96	6.78E-02	3.90E-02	9.17E-02	1.36E-02	7.25E-03	6.72E-03	6.35E-03
98	6.26E-02	3.25E-02	8.75E-02	1.42E-02	7.19E-03	6.04E-03	6.54E-03
100	6.52E-02	2.86E-02	7.70E-02	1.40E-02	7.16E-03	5.76E-03	7.13E-03

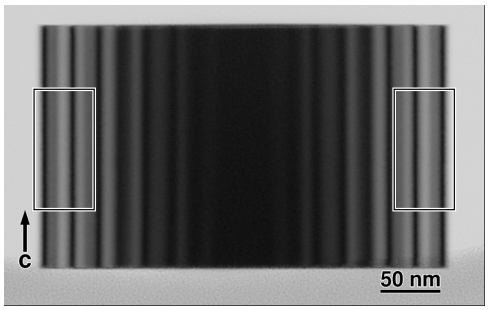

Fig. 1 Koji Nishio *et al.*

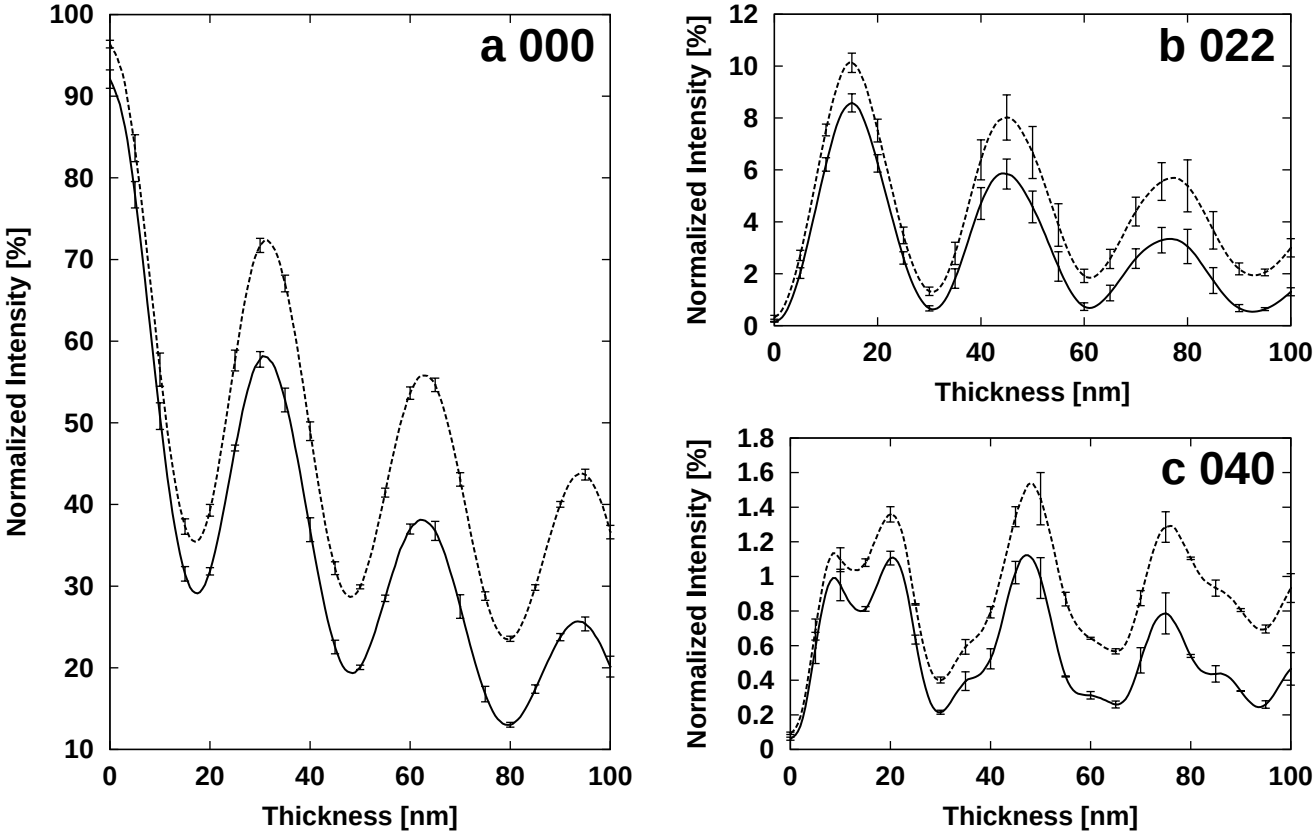

Fig. 2 Koji Nishio *et al.*

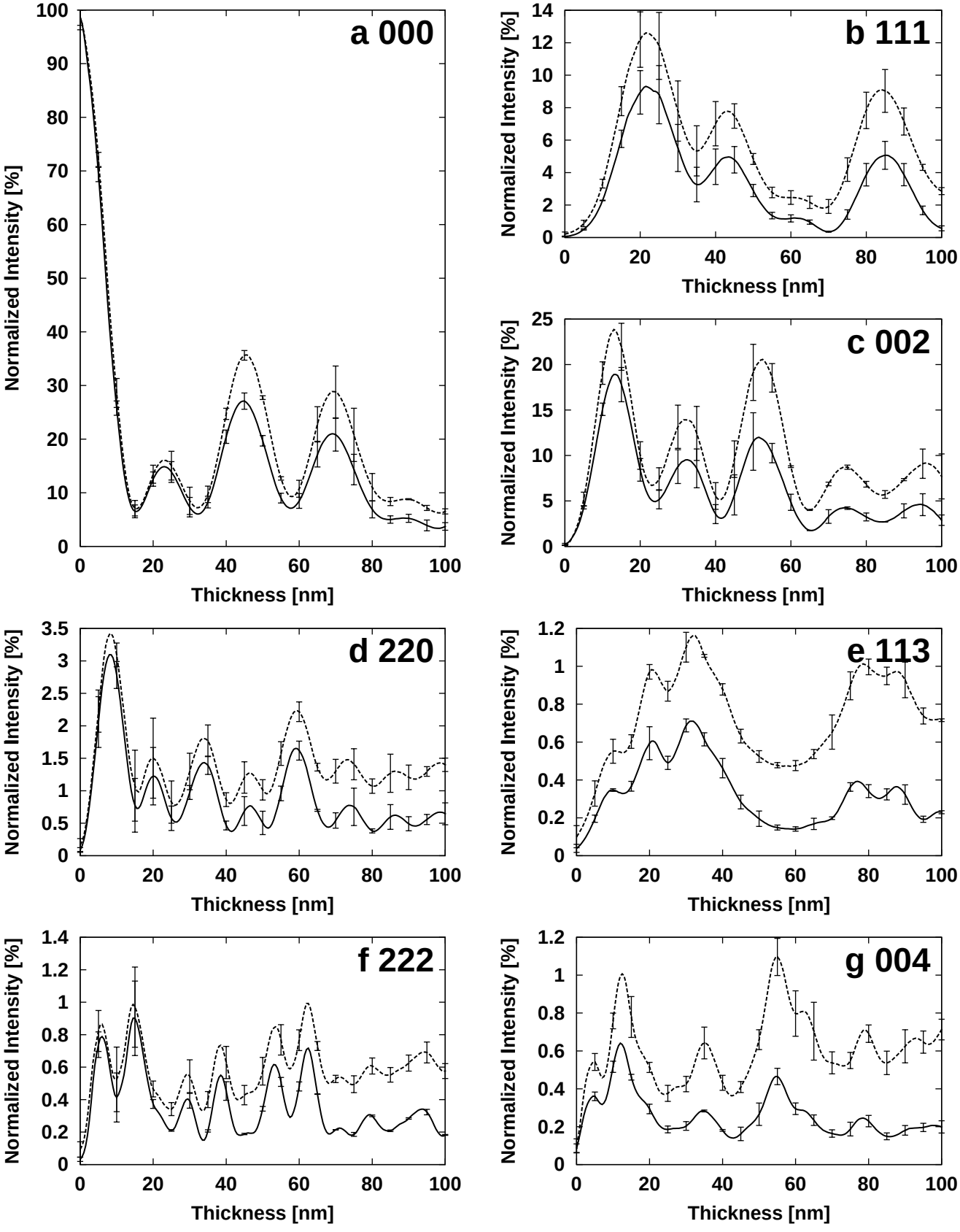

Fig. 3 Koji Nishio *et al.*

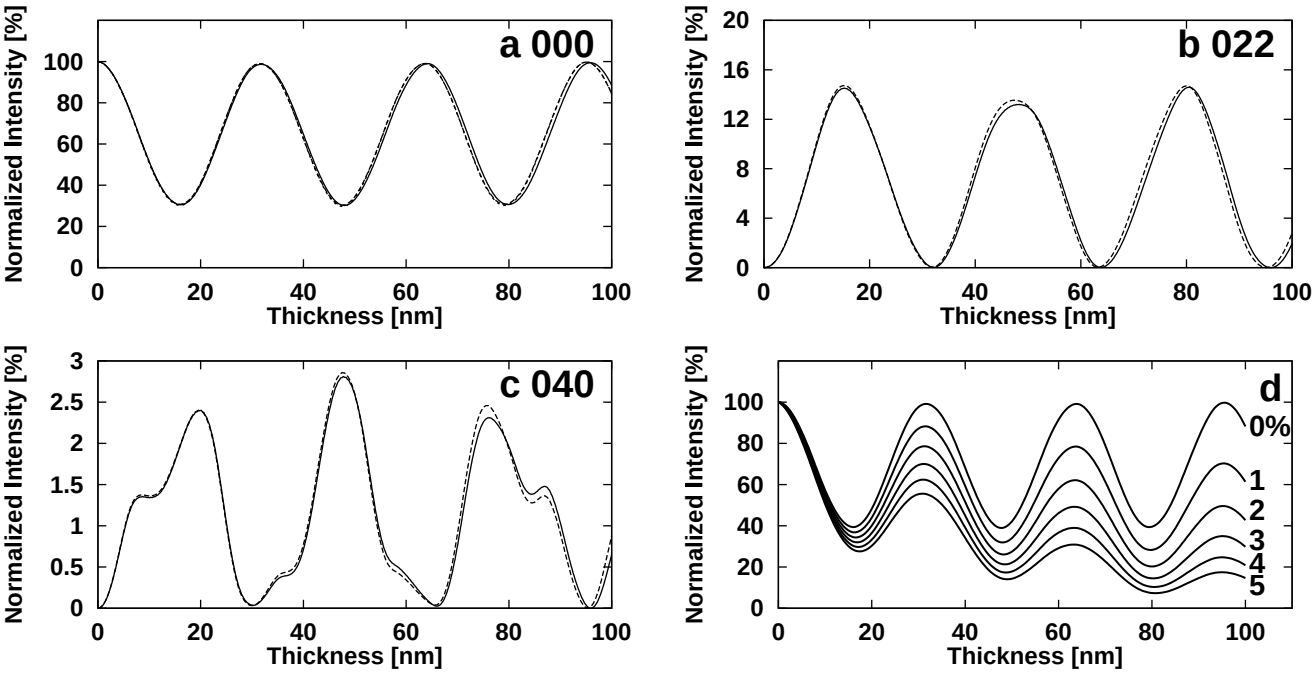

Fig. 4 Koji Nishio *et al.*

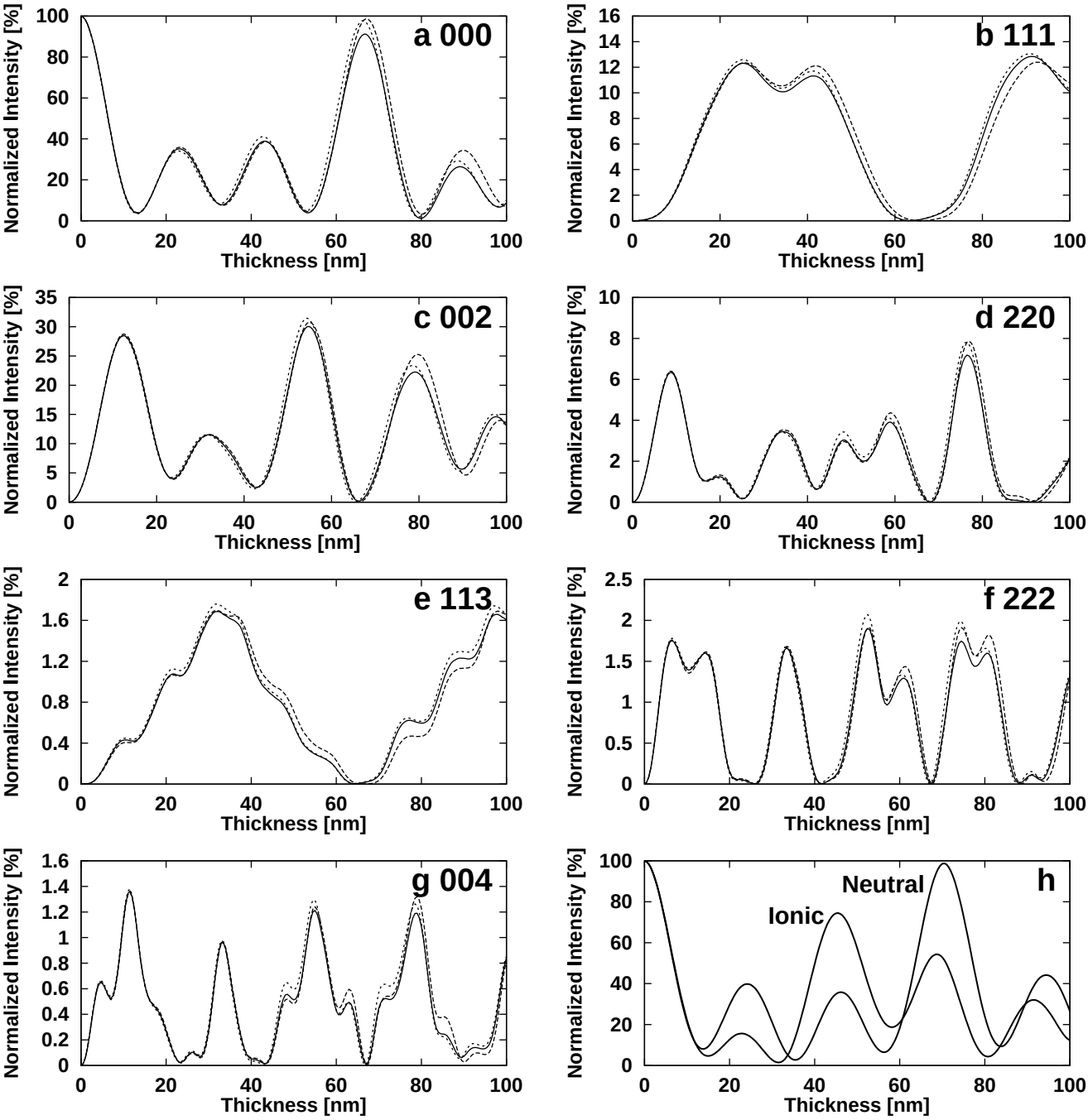

Fig. 5 Koji Nishio *et al.*

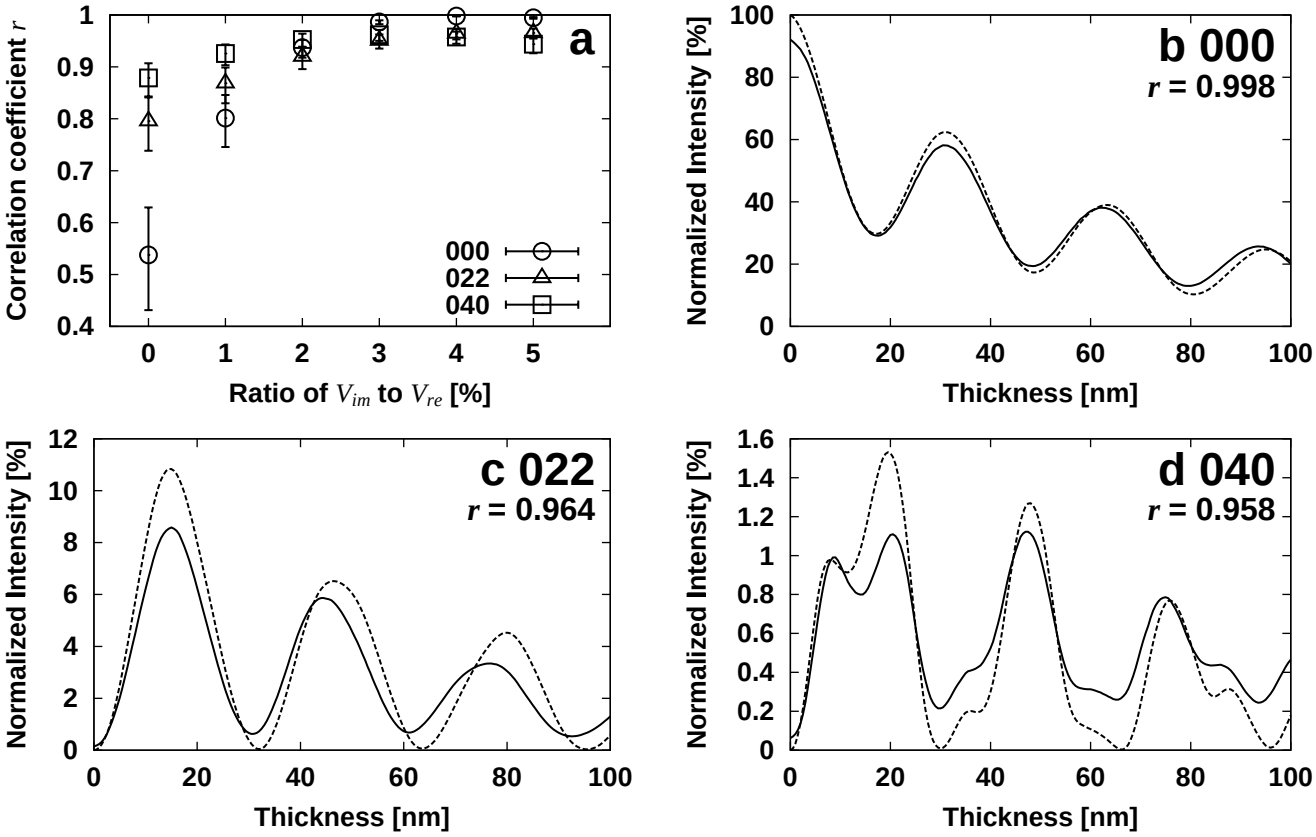

Fig. 6 Koji Nishio *et al.*

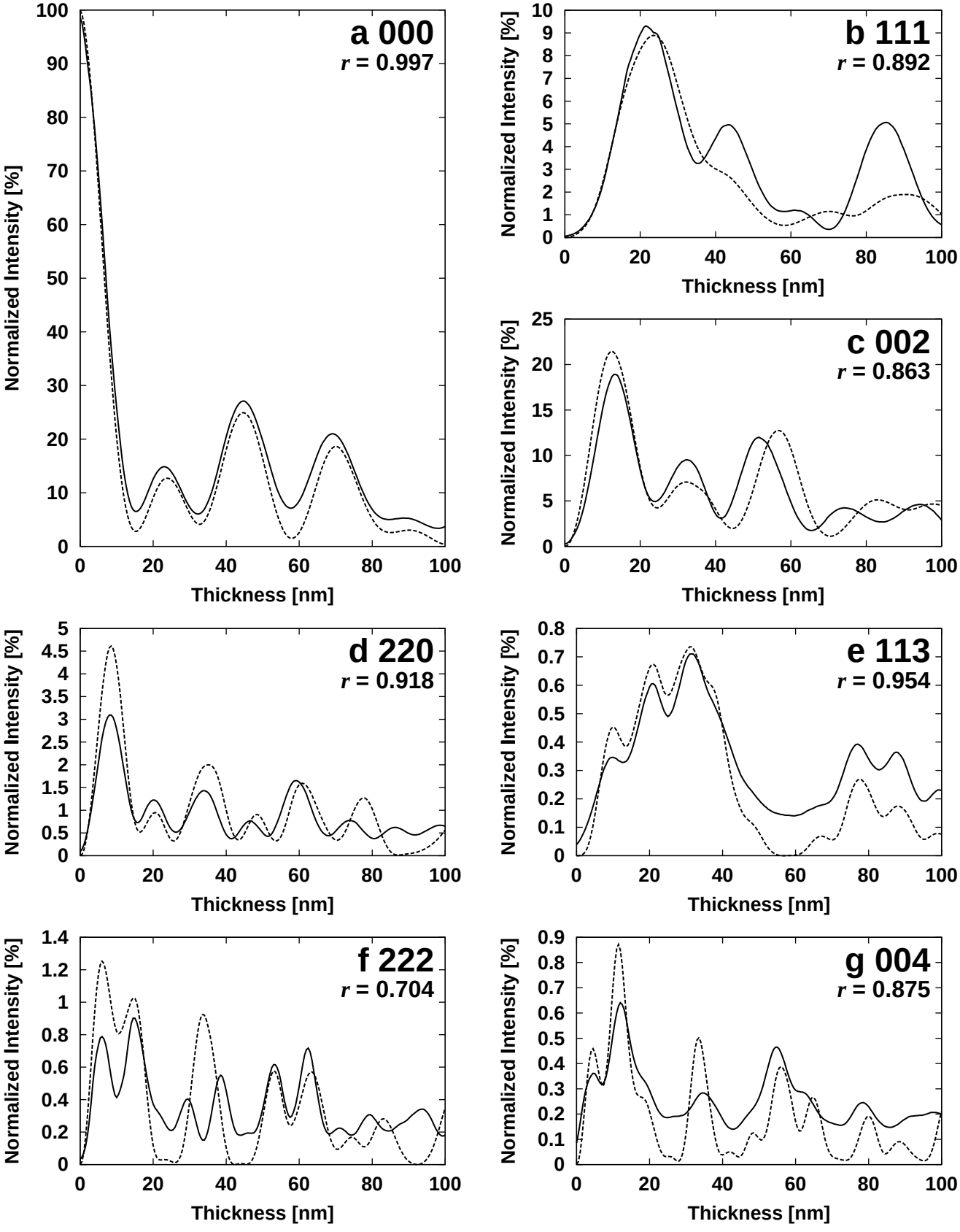

Fig. 7 Koji Nishio *et al.*